Insights into the Lithium Nucleation and Plating/Stripping Behavior in Ionic Liquid-based Electrolytes

Dominik Stępień,[1,2] Beatrice Wolff,[3,4] Thomas Diemant,[1,2] Guk-Tae Kim,[1,2] Florian Hausen,[3,4,*] Dominic Bresser [1,2,*] and Stefano Passerini [1,2,5,*]

[1] *Helmholtz Institute Ulm (HIU), 89081 Ulm, Germany*

[2] *Karlsruhe Institute of Technology (KIT), 76021 Karlsruhe, Germany*

[3] *Institute of Energy and Climate Research IEK-9, Forschungszentrum Jülich GmbH, 52425 Jülich, Germany*

[4] *Institute of Physical Chemistry, RWTH Aachen University, 52074 Aachen, Germany*

[5] *Sapienza University of Rome, Chemistry Department, Piazzale A. Moro 5, 00185 Rome, Italy*

*** Corresponding authors:**

dominic.bresser@kit.edu ; stefano.passerini@kit.edu ; f.hausen@fz-juelich.de

Keywords: ionic liquid electrolyte; electrolyte additive; zero excess; lithium-metal battery; atomic force microscopy

Abstract

Rechargeable lithium-metal batteries (LMBs) are anticipated to enable enhanced energy densities, which can be maximized when minimizing the amount of excess lithium in the cell down to zero, also referred to as “zero excess” LMBs. In this case, the only source of lithium is the positive electrode active material – just like in lithium-ion batteries. However, this requires the fully reversible deposition of metallic lithium, i.e., a Coulombic efficiency (CE) approaching 100%. Herein, the lithium plating from ionic liquid-based electrolytes, composed of *N*-butyl-*N*-methyl pyrrolidinium bis(fluorosulfonyl)imide ($PYR_{14}FSI$) and lithium bis(trifluoromethanesulfonyl)imide (LiTFSI) as conducting salt, on nickel current collectors is investigated *via* a comprehensive set of electrochemical techniques coupled with *operando* and *in situ* atomic force microscopy and *ex situ* X-ray photoelectron spectroscopy. The investigation involves the use of fluoroethylene carbonate (FEC) as electrolyte additive. The results show that an elevated LiTFSI concentration leads to a lower overpotential for the lithium nucleation and a more homogeneous deposition. The incorporation of FEC results in a further lowered overpotential and stabilized solid electrolyte interphase, enabling a substantially enhanced CE.

1. Introduction

Driven by the demand for batteries with high energy density in electric vehicles and other mobile devices, state-of-the-art lithium-ion batteries (LIBs) are approaching their limits.[1] Therefore, lithium-metal batteries (LMBs) are considered as the next-generation battery technology to achieve substantially higher energy densities.[1–4] The lithium-metal negative electrode is characterized by a very low electrochemical potential (-3.04 V vs. the standard hydrogen electrode, SHE) and high theoretical capacity (3860 mAh g^{-1}).[2] To fully use these benefits, however, a minimum excess of lithium metal is needed, ideally no excess at all. This facilitates moreover the cell assembly, since no lithium metal is needed and all lithium in the cell would be stored initially in the positive electrode active material; such cells are also referred to as "zero excess" LMBs.[5,6] This cell concept additionally diminishes the safety hazard during both the cell assembly and the cycling of the battery cell. Furthermore, it reduces the overall amount of lithium and the high cost of production for the thin lithium foil.[7] Nonetheless, many challenges still remain for the realization of "zero excess" LMBs.[5,6,8,9] Peled et al.[10] have shown that the Li metal spontaneously reacts with non-aqueous electrolytes to form a solid electrolyte interphase (SEI), an ideally purely ion conducting layer. For LMBs, the SEI is crucial to suppress further parasitic reactions, dendrite formation and, hence, enabling the lithium electrode to achieve a sufficiently high Coulombic efficiency (CE).[11,12] Generally, the SEI should fulfill the following requirements: mechanical stability during stripping and plating, insolubility in the electrolyte, high electronic resistivity, and selective permeability for the electroactive species.[11,13] Several approaches have been investigated to stabilize the passivation layer on metallic lithium, including a modified morphology of the lithium metal[14–16] or changing the SEI composition by using different electrolytes and additives such as vinylene carbonate (VC),[17,18] vinyl ethylene carbonate (VEC),[5,19–21] or fluoroethylene carbonate (FEC).[22–26]

Generally, it appears that the use of state-of-the-art organic carbonate-based electrolytes used in LIBs is ruled out for LMBs owing to their high reactivity with lithium metal, leading to continuous electrolyte consumption and, eventually, dendrite formation.[27] A potential alternative are electrolytes based on room temperature ionic liquids (ILs), for which the formation of a rather stable SEI has been reported.[28] Additional advantageous properties are the very low volatility and flammability, an ionic conductivity of up to 10^{-3} S cm^{-1} at 20 °C, a commonly wide electrochemical stability window (ESW), and high thermal stability.[29,30] The most investigated cations for ILs used in LMBs are pyrrolidinium and imidazolium-type cations, while FSI and TFSI are the most investigated anions.[28] Compared with the imidazolium cation, pyrrolidinium is more stable against lithium metal and has a broader ESW, but compromises the ionic conductivity.[30–32] Nonetheless, $PYR_{14}FSI$ was selected for the present study, because it has already shown good performance during long-term stripping-plating tests in symmetric Li‖Li cells. In fact, the FSI anion decomposes mainly to LiF, an excellent SEI-forming compound, which prevents further parasitic reactions.[28,33,34] Furthermore, nickel was used as the current collector, since aluminum alloys with lithium metal, while the FSI anion undergoes a catalytic reaction with copper.[35]

Following these considerations, herein, we first focused on the initial plating mechanism of lithium on nickel current collectors. *Operando* atomic force microscopy (AFM) was used to reveal the height and adhesion changes of plated lithium on the nickel surface during the plating process. In addition, *ex situ* X-ray photoelectron spectroscopy (XPS) was conducted to determine the decomposition products. The electrolytes used here consist of $PYR_{14}FSI$ and LiTFSI with 9:1 and 8:2 molar ratios, in the following simply referred to as 9:1 and 8:2, respectively. A third electrolyte was also investigated, which contained 5 wt.% of FEC added to 8:2 (named 8:2FEC). The lithium morphology and surface roughness changes during plating were investigated by intermittent *in situ*

AFM measurements while the plating process was paused. Finally, the plating and stripping/plating behavior at elevated temperatures was also investigated.

2. Experimental Section

2.1 Materials

N-Methylpyrrolidine (Acros Organics) and bromobutane (Merck, 98%) were used for the synthesis of the IL after distillation under atmospheric pressure. Lithium bis(fluorosulfonyl)imide (LiFSI) (Provisco, 98%) was dried for 12 h at 80 °C under vacuum (10^{-3} bar). Lithium bis(trifluoromethanesulfonyl)imide (LiTFSI; 3M, battery grade) was dried for 12 h at 120 °C under vacuum (10^{-7} bar). Fluoroethylene carbonate (FEC; Powerlyte) was used as received. For the cell assembly, 2 cm lithium stripes (Honjo; 500 µm and 50 µm thickness) and glass microfiber filters (Whatman, GF/A) were used. Nickel foil (Fukuda, battery grade) was used as current collector. For the *ex situ* analysis, the lithium-metal electrodes were rinsed with dimethyl carbonate (DMC; Powerlyte. The $LiNi_{0.6}Co_{0.2}Mn_{0.2}O_2$ (NCM_{622}) cathodes were composed of NCM_{622} (BASF) as the active material, Super C65 (IMERYS) as conductive carbon, and polyvinylidene difluoride (PVdF; Solef 6020, Solvay) as binder. *N*-methyl-2-pyrrolidone (NMP; Sigma-Aldrich) was used as dispersant for the electrode slurry.

2.2 Electrolyte Synthesis and Preparation

All electrolyte compositions employed $PYR_{14}FSI$, which was synthesized according to the procedure reported by Montanino et al.[36] The electrolytes consisting of $PYR_{14}FSI$-LiTFSI with the ratio 9:1 and 8:2 were dried using the following procedure: 2 h at room temperature, 6 h at 50 °C and 12 h at 80 °C under vacuum (10^{-3} bar), and finally by the same procedure employing a

turbomolecular pump (10^{-7} bar). The third electrolyte, 8:2FEC, was dried according to the above-mentioned vacuum procedure, but at room temperature only.

2.3 Cell Assembly and Electrochemical Characterization

The cells were assembled in a dry room (dew point of incoming air: -70 °C) using two pieces of 10×10 cm^2 pouch foil, which were already sealed at the top, including the two nickel current collectors (width: 1 cm). Lithium metal stripes and nickel foils (2×3 cm^2) were used as the electrodes for the Li‖Ni cells. The separator was drenched with 0.2 mL electrolyte. To completely wet the separator and ensure the complete removal of (dry) air, the cells were placed under vacuum (10^{-3} bar) twice for 99 s. Then, the pouch cells were sealed. The electrodes overlapped by 1.5×2 cm^2, i.e., the active area was 3 cm^2. The NCM_{622} cathodes were composed of NMC_{622} as the active material, Super C65 as conductive additive, and PVdF as binder. The components were mixed in a weight ratio of 92:4:4. The electrode slurry containing NMP as dispersant was coated on 15 µm thick aluminum foil and dried at 60 °C for 12 h. After this initial drying, electrodes with a diameter of 12 mm were punched and vacuum-dried for 12 h at 120 °C, and subsequently pressed at 8 tons per cm^2. The average active material mass loading was 2.8 ± 0.15 mg cm^{-2}. The cell assembly was the same as for the Li‖Li cells, with the only difference that the electrodes had a diameter of 12 mm and that an aluminum stripe was used at the cathode side.

2.4 Physicochemical and Electrochemical Characterization

The viscosity of the electrolytes was measured inside the dry room by means of an Anton-Paar MCR102 rheometer equipped with a cone-plate geometry. The measurements were conducted in the range from 20 °C to 60 °C with a step size of 5 °C. An equilibration period of 15 min was set

prior to each measurement. To achieve Newtonian behavior of the fluid, the constant shear rate was set to 20 s^{-1}. The ionic conductivity was determined in the same temperature range (i.e., from 20 °C to 60 °C) using an impedance conductometer (MMates). A 0.01M KCl solution was used as standard for the calibration of the conductivity cells, comprising two platinum electrodes. After each 5 °C temperature step, the cells were equilibrated for 15 min. Multiple conductivity measurements were acquired over a period of 45 min and the average values were used. The limiting current density was measured with a potentiostat/galvanostat (Solatron 1260) employing Li‖Ni cells inside a climatic chamber (Binder). Electrochemical impedance spectroscopy (EIS) was performed in the frequency range from 0.1 mHz to 1 MHz with an excitation voltage of 10 mV using a VMP3 (BioLogic). The same instrument was also used for the plating and stripping/plating experiments.

2.5 Operando and in situ Atomic Force Microscopy

AFM was performed using a general-purpose electrochemistry cell (Bruker) and a 3-electrode setup. As working electrode, a 1×1 cm^2 piece of nickel foil was used. The counter and reference electrodes were made from a piece of lithium foil wrapped around a copper wire. The AFM (Bruker Dimension Icon) was located inside a glove box (MBraun, O_2 and H_2O <0.1 ppm). A plating current of -80 µA cm^{-2} was applied *via* a potentiostat (Biologic SP300) for a total duration of 60 min. The plating was monitored *operando* by AFM using line scans with the slow scan speed axis switched off, thereby mapping the time evolution of a single scan line. After 10 min, the plating was interrupted to record a 5×5 μm^2 *in situ* map of the surface. All AFM images were recorded in a force spectroscopy mode (PeakForce Quantitative Nanomechanical Mapping). The calibration of the tip radius was conducted on highly oriented pyrolytic graphite (HOPG) and

polystyrene reference samples (Bruker). The elastic modulus was determined according to the Derjaguin-Muller-Toporov model.

2.6 Ex situ Analysis

For the *ex situ* analysis, the Li_{Ni} electrodes were rinsed five times with 0.1 mL of DMC to remove any residual traces of the electrolyte. The surface morphology was investigated *via* scanning electron microscopy (SEM; Crossbeam XB340, Zeiss). The chemical composition of the surface was investigated by X-ray photoelectron spectroscopy (XPS) in an SPECS UHV system with monochromatic Al Kα radiation (400 W, 15 kV) and a PHOIBOS 150 energy analyzer equipped with a micro-channel plate and delay line detector to collect the photoelectrons. The measurements were done at a take-off angle of 45° and a pass energy of 30 eV for the detail scans. For binding energy calibration of the spectra, the C1s peak of hydrocarbon species (C-C/C-H) was set to 284.8 eV. The peak fitting of the data was carried out with CasaXPS, using Shirley-type backgrounds and Gaussian-Lorentzian peak shapes (70% Gaussian and 30% Lorentzian, GL30). For the peak fit in the S 2p region, peak doublets with the well-known intensity ratio (2:1) and spin-orbit splitting (Δ = 1.18 eV) were used.

3. Results and Discussion

3.1 Physicochemical Characterization of the Electrolytes

The ionic transport properties of the IL-based electrolytes were investigated in the temperature range from 20 to 60 °C (**Figure 1**). The influence of the concentration of the conducting salt LiTFSI was studied employing two different $PYR_{14}FSI$ to LiTFSI molar ratios, viz., 9:1 and 8:2. Additionally, the effect of adding FEC to 8:2 was investigated. **Figure 1a** shows the correlation of the ionic transport properties with the viscosity. As expected for liquid electrolytes, upon

increasing temperatures the viscosity decreases following the Vogel-Fulcher-Tammann behavior. Accordingly, the ionic conductivity increases following the same law (**Figure 1b**), while the limiting current density (which is related to the Li-ion mobility) shows a rather linear increase (**Figure 1c**). The electrolyte composition, i.e., the molar ratio, is also seen to influence the transport properties. The higher $PYR_{14}FSI$ ratio of 9:1 generally shows a lower viscosity and higher ionic conductivity at any temperature.[37] However, the higher LiTFSI molar ratio of 8:2 shows a significantly increased limiting current density, despite a higher viscosity. This behavior is attributed to the weaker interaction between the anions and the Li^+ cations owing to the increased fraction of TFSI anions, disrupting the organization/crystallization of the liquid due to the more delocalized charge of the bulkier molecule compared to the FSI anion.[38] Surprisingly, the addition of the low-viscosity solvent FEC does not have any significant effect on the viscosity and a rather minor effect on the ionic transport properties. In fact, only a slight increase of the limiting current density is observed at elevated temperatures. The latter is likely due to the enhanced Brownian motion of the ionic species, which allows more FEC to coordinate towards the Li^+ cation, thus, increasing the Li^+ transfer number.

3.2 Operando and in situ Atomic Force Microscopy

To achieve a high CE, a thorough understanding of the initial lithium nucleation phase is crucial. For this purpose, we recorded *operando* AFM line scans which were correlated to voltage vs. time profiles. The AFM images were obtained with the slow scan axis off and, hence, represent the evolution of the identical scan line with time and can be directly compared with the applied voltage. The results for the 8:2FEC electrolyte are displayed in **Figure 2a** (cf. **Figure S1** for 9:1 and 8:2). All three electrolytes showed a similar behavior in the height and adhesion profiles. The

initial nucleation phase extends from the open circuit potential (OCP, ~3 V) until the potential becomes lower than 0 V vs. Li^+/Li, i.e., stages ① and ② in **Figure 2a**. Initially, a fast electrode polarization occurs till the cell potential reaches 1.5 V vs. Li^+/Li. Afterwards the potential decay slows down substantially. The phenomena occurring below 1.5 V can be summarized as follows: (i) decomposition of the electrolyte, which is examined by AFM scans, and (ii) the reaction of the lithium cations with the native nickel oxide layer on the current collector surface. The AFM line scans reveal bidimensional changes in the height and the adhesion of the electrode surface. During the nucleation phase, corresponding to the potential decay region from ① to ②, the adhesion measurements evidence mostly the nickel surface for the initial 15 s. Afterwards, a lower adhesion of the surface occurs, as indicated by the shift to a brighter color. The height scan also reveals slight changes. These experimental evidences point to the occurrence of electrolyte decomposition, resulting in the formation of decomposition products on the nickel surface. This is also confirmed by *ex situ* XPS measurements on the electrode surface before and after the initial nucleation phase (**Figure 2b**). **Figure 2b①** shows the F1s and S2p spectra of the pristine electrodes immersed in the three electrolytes. Only features associated to the FSI and TFSI anion are observed, indicating that all electrolytes are stable in contact with the nickel current collector at open circuit conditions.[39] The comparison with the XPS data collected after the initial nucleation phase, i.e., after the polarization of the current collector (**Figure 2b②**), shows that the features associated to the pristine anions have much lower intensities, while additional peaks assigned to the presence of LiF (F1s) as well as SO_3^{2-} and Li_2S (S2p) show up. Hence, the decomposition of the electrolyte results in the formation of an SEI layer coating the current collector. For the electrolytes without FEC additive, these new peaks in the F1s and S2p regions are more apparent for 9:1 than for 8:2. A potential explanation might be the time frame of the initial nucleation phase, which depends on

the supersaturation of the Li cations. In fact, following the findings concerning the limiting current density (**Figure 1c**), the 8:2 electrolyte reaches supersaturation faster than the 9:1 electrolyte, meaning that nucleation sets in earlier, thus, preventing additional reductive electrolyte decomposition (such as that of the pyrrolidinium cation based on the C=C species in the C1s spectra seen in **Figure S2②**). Interestingly for the electrolyte with FEC additive (8:2FEC), the peaks related to electrolyte decomposition products are even more pronounced, especially the LiF peak. This presumably originates from the decomposition of FEC, which is electrochemically less stable than FSI and TFSI.[40] The FEC decomposition might trigger then also the decomposition of the two anions (e.g., by intermediately formed decomposition species and/or a different electrochemical stability of the remaining coordination shell of the lithium cation), as also the SO_3^{2-} and Li_2S (S2p) peaks are more pronounced than in the other two cases.

In the second phase (i.e., from ② to ③), the Li-ion concentration at the electrode/electrolyte interface has reached supersaturation and overcomes the nucleation barrier resulting in the actual deposition of lithium metal. The height profile (**Figure 2a**, top panel) shows small peaks (new bright yellow spots) appearing, which increase with time and can be assigned to lithium nuclei formation on the nickel surface over the first two minutes of plating. This indicates that lithium nucleation is a progressive rather than an instantaneous process. Throughout the deposition process a stable polarization of about -23 mV vs. Li^+/Li is observed (**Figure 2a**). The trend towards low adhesion of the initial nucleation phase is maintained and still related to the SEI (now on the plated lithium metal). The most remarkable feature observed by *ex situ* XPS after long-term plating (**Figure 2b③**) is the high intensity of the LiF peak in the case of 9:1, indicating that the plating was accompanied by significant further electrolyte decomposition – presumably owing to the generally lower lithium concentration at the electrode | electrolyte interface.

The actual lithium nuclei growth can be even better observed from the *in situ* AFM mapping presented in **Figure 3**, with the corresponding voltage profiles displayed in **Figure S3** and images obtained with an optical camera in **Figure S4**. The 9:1 electrolyte, with its lower amount of lithium salt, leads to a rather mossy-like lithium morphology with a rather high surface area. Upon further plating, the overall morphology of the deposited lithium does not significantly change. However, after 20 min of plating, a large particle can be seen in the upper right corner, which indicates the formation of dendritic lithium deposits. Differently, the other two electrolytes with a higher lithium salt concentration show particle-like lithium deposition. Besides, nucleation seems to preferably occur on the elevated spots of the nickel current collector, indicating that a smooth current collector surface plays an important role for achieving a smooth lithium metal deposition. In more detail, for 8:2, the particles are growing into different sizes and new nuclei appear on the surface for up to 30 min, resulting in increased surface area. Nonetheless, also the existing particles continue to grow, eventually, resulting in the smoothening of the plating surface. In the case of 8:2FEC, the lithium particles are better distributed on the surface and show a more homogeneous size distribution (as highlighted also in **Figure S5**, showing a larger area of 20×20 μm^2). Moreover, there is no evidence of new nuclei appearing after 10 min of plating. Biswal et al.[41] reported that the addition of FEC to an organic carbonate-based electrolyte has a beneficial effect on the surface energy and ion diffusion on the surface, which in turn results in a smoother morphology of the lithium metal layer.

To analyze the surface roughness in more detail for all three electrolyte systems, the roughness was calculated for each image as the root mean square of the height and normalized to zero by subtracting the roughness of the respective pristine nickel surface (**Figure 4**). The maximum change in roughness differs for the various electrolytes in the following order: 9:1 > 8:2 > 8:2FEC.

More precisely, in the case of 9:1, the surface roughness initially increases, but then remains rather constant, indicating that the initial increase in roughness is maintained and the continuing plating does not have a significant impact on the lithium morphology, which is in line with the observations from the AFM mapping. Differently, the surface roughness of the 8:2 sample initially increases, but then decreases, which is in good agreement with the initial particle-like lithium deposition, followed by their continuous growth and the deposition of additional lithium particles, eventually resulting in a smoothening surface. The 8:2FEC electrolyte, in contrast, yields the lowest surface roughness, which is slightly growing and generally consistent with the observation of continuously growing, well-distributed lithium particles. A similar effect of FEC has been observed by *operando* electron paramagnetic resonance spectroscopy, indicating a more homogenous and less mossy structured lithium deposition.[26]

To corroborate the *in situ* and *operando* AFM results, the measurements were repeated in common pouch cells (**Figure S6**). These cells show similar potential profiles and polarization behavior (9:1 > 8:2 > 8:2FEC) for the three electrolytes (**Figure S6a**). It may be noted that the higher surface roughness (and presumably surface area) observed for 9:1 does apparently not result in a lower polarization. Instead, the lithium salt concentration – and, thus, lithium concentration at the electrode | electrolyte interface – in combination with the composition of the SEI (favorable in the presence of FEC) are the dominating impact factors. Furthermore, the morphology of the lithium deposits, as observed from the subsequently performed *ex situ* SEM analysis (**Figure S6b-d**) resembles very well the *in situ* AFM mapping results with several large globular lithium deposits, which potentially serve as onset for dendrite growth (**Figure S6b**), a much more homogeneous lithium deposition in the case of 8:2 (**Figure S6c**), and a very smooth lithium surface in the case

of 8:2FEC (**Figure S6d**), which is perfectly in line with the determination of the surface roughness determined from the *in situ* AFM mapping.

3.3 Lithium Plating and Stripping at Varying Temperatures

The plating behavior was further studied by varying the measurement temperature from 20 °C to 60 °C, while keeping the current density constant at 80 µA cm^{-2}. The investigation of the initial nucleation phase is presented in **Figure 5**. The comparison of the potential profiles recorded at 20 °C (**Figure 5a**) and at 60 °C (**Figure 5b**) shows that at elevated temperatures the initial nucleation phase is prolonged. This is due to the generally lower electrochemical stability of these electrolytes at higher temperatures, leading to an increased reductive decomposition and, hence, a lower initial CE. Nevertheless, the electrolytes with the higher lithium salt concentration, i.e., 8:2 with and without FEC, reach the supersaturation state in a shorter time, which agrees with the AFM line scan experiments reported in **Figure 2**. Interestingly, the impact of adding FEC is reduced at 60 °C, presumably owing to the fact that it decomposes already at relatively higher potentials and rather rapidly in either case. During the subsequent plating the overpotential is generally lower at 60 °C owing to the increased ionic conductivity of the electrolytes (due to the lower viscosity) and the enhanced electrode kinetics (cf. **Figure 1**). Independent from the temperature, though, 8:2 and 8:2FEC show a lower overpotential for the lithium plating. After 10 h of plating, all cells were stopped and disassembled to investigate the morphology of the lithium deposition by *ex situ* SEM **(Figure 5d-i**; an SEM micrograph of the pristine nickel foil is presented as well in **Figure 5j** for the sake of comparison). The results obtained at 20 °C (**Figure 5d-f**) are generally in good agreement with the data presented in **Figure S6**, revealing some larger particles for 9:1 and a smoother surface for 8:2 and 8:2FEC. At 60 °C, these differences are even more

pronounced with several (very) large particles in the case of 9:1 (**Figure 5g**) and much smaller particles of a very homogeneous size and local distribution in the case of 8:2 (**Figure 5h**) and 8:2FEC (**Figure 5i**). In general, these findings indicate a pronounced "tip-type" lithium deposition at elevated temperatures, which is most pronounced for a lower lithium salt concentration,[42] as the lithium concentration at the electrode | electrolyte interface is smaller, resulting in the formation of fewer lithium nuclei on the surface and, eventually, larger (dendrite-like) lithium deposits.

The corresponding investigation upon prolonged plating and stripping experiments using lithiated nickel electrodes (Li_{Ni}) in combination with lithium-metal electrodes (referred to as Li_{Ni}‖Li cells) is presented in **Figure 6**. At 20 °C (**Figure 6a-b**), all three electrolytes show a rather stable overpotential. In the case of the more concentrated electrolytes (8:2 and 8:2FEC) the overpotential is very similar, while it is higher for 9:1. This is attributed to the more sluggish Li-ion transport in the electrolyte, although also an influence of the interphase formed cannot be excluded. At 60 °C, the overall polarization is generally lower due the decreased viscosity and higher ionic conductivity. However, it gradually increases for 9:1, indicating an increase of the interfacial charge transfer resistance upon cycling due to an increased electrolyte decomposition and the consequently increasing thickness of the interphase. In contrast, the addition of FEC leads to a stable overpotential at 60 °C, which is also lower compared to that observed for 9:1 and 8:2. It is known that the addition of FEC results in a polymer-rich SEI, which has been reported to be beneficial for the Li-ion transport in the interphase.[25,43] This effect of FEC is seen especially at higher temperatures, as its decomposition and the formation of polymeric products is presumably favored in such case, while the polymer-comprising interphase itself has a higher Li-ion conductivity. The subsequent *ex situ* SEM investigation of the Li_{Ni} electrodes after 100 h of lithium stripping and plating at 20 °C corroborates the previous findings of a more homogeneous lithium

deposition in the case of 8:2 and 8:2FEC (**Figure 6d-e**). At 60 °C (**Figure 6f-h**) the surface appears generally smoother for all three electrolytes, which is in line with previous work reporting a faster growth of pre-existing particles at lower temperatures, which increases the probability of the initiation of dendrite growth.[44] This can also be seen in **Figure S7**, displaying lithium stripping/plating tests at an elevated current density of 160 μA cm^{-2}, where a short circuit was observed for 9:1 at 20 °C (**Figure S7a** – see also **Figure 3**) and an increasing overpotential at 60 °C (**Figure S7b**), while it remained stable for the higher lithium salt concentrations and was generally the lowest for 8:2FEC.

For a further confirmation of the beneficial effect of FEC, EIS was conducted after the initial plating step every 12 h over a two-day rest period in OC conditions (**Figure 7a,b**). In the case of 8:2 (**Figure 7a**), the impedance increases continuously, indicating further electrolyte decomposition at the electrode | electrolyte interface, while it remains essentially stable for 8:2FEC (**Figure 7b**). The superior stability of the interphase formed in presence of FEC is also apparent from the comparison of Li_{Ni}||Li cells cycled with and without such 2 days of rest after the initial plating (**Figure 7c, d**). In fact, for 8:2, the overpotential is higher when including such rest step (**Figure 7c**), while it remains the same for 8:2FEC (**Figure 7d**).

3.4 Galvanostatic Cycling of Li||NCM_{622} Cells

Finally, we performed galvanostatic cycling on Li||NCM_{622} cells to assess the feasibility of utilizing the IL-based electrolytes in LMBs (**Figure 8**). The initial C rate test demonstrates that a higher lithium salt concentration enables higher capacities at 1C in the order 9:1 < 8:2 < 8:2FEC due to the higher Li^+ mobility and superior charge transport kinetics at the interface, as evidenced by the reduced SEI and charge transfer resistance in **Figure 7**. Furthermore, we observed an

increase in Coulombic efficiency in the same order, which is assigned to the different surface morphology of the lithium metal when increasing the lithium salt concentration and adding FEC, while especially the latter apparently also has a stabilizing effect on the interphase formed. Additionally, the electrolyte with a 9:1 ratio showed a gradual decrease in capacity upon the eventual constant current cycling at 0.3C, presumably due to the continuous electrolyte decomposition at the Li | electrolyte interface, though also reactions at the interface with the NCM_{622} cathode might play a role.

4. Conclusions

The comparative investigation of IL-based electrolytes with a different lithium salt concentration and in presence of FEC as electrolyte additive shows that both have a substantial impact on the lithium nucleation and growth. Generally, a higher lithium concentration (in the bulk electrolyte and, as a consequence at the electrode | electrolyte interface) leads to less reductive electrolyte decomposition as well as a smoother and more homogeneous lithium deposition, which is further favored when adding FEC, as also reflected in the superior CE observed for the Li‖NCM_{622} cells. More specifically, Li plating from 9:1 exhibits a mossy-like lithium morphology, while the use of 8:2 and 8:2FEC results in a particle-like growth of the lithium metal. The addition of FEC yields a substantially decreased surface roughness, lower and stabilized overpotential (especially at elevated temperatures), and a more stable interphase after the initial lithium plating, as indicated by a constant impedance during rest and maintained overpotential after such rest step. We may anticipate that these findings will contribute to the design of suitable (potentially liquid) electrolyte systems for (“zero excess”) lithium-metal batteries.

Supporting Information

Additional *operando* AFM line scans; voltage vs. time profiles; digital images; AFM mappings; SEM micrographs of the plated lithium; stripping/plating tests at higher current densities.

Author Contributions

D.S. performed the electrochemical characterization and the SEM measurements, analyzed all the data, and drafted the manuscript. B.W. performed the AFM experiments and revised the manuscript. T.D. performed the XPS measurements and revised the manuscript. G.-T.K. conceptualized the activities and supervised the experimental work. F.H. provided funding, conceptualized and coordinated the activities for the AFM experiments and revised the manuscript. D.B. and S.P. conceptualized and coordinated the activities, provided funding for the work, and revised the manuscript.

Conflict of Interest

The authors declare no competing financial interest.

Acknowledgement

The authors would like to acknowledge the financial support from the Helmholtz Association and the German Federal Ministry of Education and Research (BMBF) within the LILLINT (03XP0225D and 13XP0225C) and LILLINT-2 project (03XP0511E and 13XP0511B).

References

(1) Thackeray, M. M.; Wolverton, C.; Isaacs, E. D. Electrical Energy Storage for Transportation - Approaching the Limits of, and Going beyond, Lithium-Ion Batteries. *Energy Environ. Sci.* **2012**, *5* (7), 7854–7863.

(2) Owens, B. B.; Skarstad, P. M. Ambient Temperature Solid State Batteries. *Solid State Ionics* **1992,** *53-56*, 665-672.

(3) Asenbauer, J.; Eisenmann, T.; Kuenzel, M.; Kazzazi, A.; Chen, Z.; Bresser, D. The Success Story of Graphite as a Lithium-Ion Anode Material-Fundamentals, Remaining Challenges, and Recent Developments Including Silicon (Oxide) Composites. *Sustainable Energy Fuels*, **2020**, *4*, 5387.

(4) Bresser, D.; Hosoi, K.; Howell, D.; Li, H.; Zeisel, H.; Amine, K.; Passerini, S. Perspectives of Automotive Battery R&D in China, Germany, Japan, and the USA. *J. Power Sources* **2018**, *382*, 176–178.

(5) Geng, K.; Eisenmann, T.; Parmar, R.; Rezvani, J.; Gunnella, R.; Amati, M.; Gregoratti, L.; Stepien, D.; Diemant, T.; Bresser, D. Impact of a PEO-Based Interphase at the Negative Electrode of "Zero Excess" Lithium-Metal Batteries. *J. Electrochem. Soc.* **2022**, *169* (11).

(6) Qian, J.; Adams, B. D.; Zheng, J.; Xu, W.; Henderson, W. A.; Wang, J.; Bowden, M. E.; Xu, S.; Hu, J.; Zhang, J. G. Anode-Free Rechargeable Lithium Metal Batteries. *Advanced Functional Materials*. **2016**, 7094–7102.

(7) Xie, Z.; Wu, Z.;An, X.; Yue, X.; Wang, J.; Abudula, A.; Guan, G. Anode-free rechargeable lithium metal batteries: Progress and prospects. *Energy Storage Materials.* **2020,** *32*, 386-401.

(8) Howlett, P. C.; Izgorodina, E. I.; Forsyth, M.; MacFarlane, D. R. Electrochemistry at

Negative Potentials in Bis(Trifluoromethanesulfonyl) Amide Ionic Liquids. *Zeitschrift fur Phys. Chemie* **2006**, *220* (10–11), 1483–1498.

(9) Horstmann, B.; Shi, J.; Amine, R.; Werres, M.; He, X.; Jia, H.; Hausen, F.; Cekic-Laskovic, I.; Wiemers-Meyer, S.; Lopez, J.; Galvez-Aranda, D.; Baakes, F.; Bresser, D.; Su, C. C.; Xu, Y.; Xu, W.; Jakes, P.; Eichel, R. A.; Figgemeier, E.; Krewer, U.; Seminario, J. M.; Balbuena, P. B.; Wang, C.; Passerini, S.; Shao-Horn, Y.; Winter, M.; Amine, K.; Kostecki, R.; Latz, A. Strategies towards Enabling Lithium Metal in Batteries: Interphases and Electrodes. *Energy Environ. Sci.* **2021**, *14* (10), 5289–5314.

(10) Peled, E. Film Forming Reaction at the Lithium/Electrolyte Interface. *J. Power Sources* **1983**, *9* (3), 253–266.

(11) Cheng, X. B.; Zhang, R.; Zhao, C. Z.; Wei, F.; Zhang, J. G.; Zhang, Q. A Review of Solid Electrolyte Interphases on Lithium Metal Anode. *Adv. Sci.* **2015**, *3* (3), 1–20.

(12) He, X.; Bresser, D.; Passerini, S.; Baakes, F.; Krewer, U.; Lopez, J.; Mallia, C. T.; Shao-Horn, Y.; Cekic-Laskovic, I.; Wiemers-Meyer, S.; Soto, F. A.; Ponce, V.; Seminario, J. M.; Balbuena, P. B.; Jia, H.; Xu, W.; Xu, Y.; Wang, C.; Horstmann, B.; Amine, R.; Su, C. C.; Shi, J.; Amine, K.; Winter, M.; Latz, A.; Kostecki, R. The Passivity of Lithium Electrodes in Liquid Electrolytes for Secondary Batteries. *Nat. Rev. Mater.* **2021**, *6* (11), 1036–1052.

(13) Peled, E.; Menkin, S. Review — SEI : Past , Present and Future Review. *J. Electrochem. Soc.* **2017**, *164* (7), A1703.

(14) Zhang, R.; Li, N. W.; Cheng, X. B.; Yin, Y. X.; Zhang, Q.; Guo, Y. G. Advanced Micro/Nanostructures for Lithium Metal Anodes. *Adv. Sci.* **2017**, *4* (3), 1600445.

(15) Wang, S. H.; Yin, Y. X.; Zuo, T. T.; Dong, W.; Li, J. Y.; Shi, J. L.; Zhang, C. H.; Li, N. W.; Li, C. J.; Guo, Y. G. Stable Li Metal Anodes via Regulating Lithium Plating/Stripping in

Vertically Aligned Microchannels. *Adv. Mater.* **2017**, *29* (40), 1–8.

(16) Wang, A.; Zhang, X.; Yang, Y. W.; Huang, J.; Liu, X.; Luo, J. Horizontal Centripetal Plating in the Patterned Voids of Li/Graphene Composites for Stable Lithium-Metal Anodes. *Chem* **2018**, *4* (9), 2192–2200.

(17) Kühn, S. P.; Pfeiffer, F.; Bela, M.; Rodehorst, U.; Weintz, D.; Stan, M.; Baghernejad, M.; Winter, M.; Cekic-Laskovic, I. Back to the Basics: Advanced Understanding of the as-Defined Solid Electrolyte Interphase on Lithium Metal Electrodes. *J. Power Sources* **2022**, *549*, 232118.

(18) Ota, H.; Shima, K.; Ue, M.; Yamaki, J. ichi. Effect of Vinylene Carbonate as Additive to Electrolyte for Lithium Metal Anode. *Electrochim. Acta* **2004**, *49* (4), 565–572.

(19) Zhang, Q.; Liu, S.; Lin, Z.; Wang, K.; Chen, M.; Xu, K.; Li, W. Highly Safe and Cyclable Li-Metal Batteries with Vinylethylene Carbonate Electrolyte. *Nano Energy* **2020**, *74*, 104860.

(20) Yang, Y.; Xiong, J.; Lai, S.; Zhou, R.; Zhao, M.; Geng, H.; Zhang, Y.; Fang, Y.; Li, C.; Zhao, J. Vinyl Ethylene Carbonate as an Effective SEI-Forming Additive in Carbonate-Based Electrolyte for Lithium-Metal Anodes. *ACS Appl. Mater. Interfaces* **2019**, *11*, 6118-6125.

(21) He, J.; Wang, H.; Zhou, Q.; Qi, S.; Wu, M.; Li, F.; Hu, W.; Ma, J. Unveiling the Role of Li^+ Solvation Structures with Commercial Carbonates in the Formation of Solid Electrolyte Interphase for Lithium Metal Batteries. *Small Methods* **2021**, *5* (8), 1–10.

(22) Markevich, E.; Salitra, G.; Chesneau, F.; Schmidt, M.; Aurbach, D. Very Stable Lithium Metal Stripping-Plating at a High Rate and High Areal Capacity in Fluoroethylene Carbonate-Based Organic Electrolyte Solution. *ACS Energy Lett.* **2017**, *2* (6), 1321–1326.

(23) Umeda, G. A.; Menke, E.; Richard, M.; Stamm, K. L.; Wudl, F.; Dunn, B. Protection of Lithium Metal Surfaces Using Tetraethoxysilane. *J. Mater. Chem.* **2011**, *21* (5), 1593–1599.

(24) Dai, H.; Gu, X.; Dong, J.; Wang, C.; Lai, C.; Sun, S. Stabilizing Lithium Metal Anode by Octaphenyl Polyoxyethylene-Lithium Complexation. *Nat. Commun.* **2020**, *11* (1), 643.

(25) Xu, N.; Shi, J.; Liu, G.; Yang, X.; Zheng, J.; Zhang, Z.; Yang, Y. Research Progress of Fluorine-Containing Electrolyte Additives for Lithium Ion Batteries. *J. Power Sources Adv*. **2021**, *7*, 100043.

(26) Wandt, J.; Marino, C.; Gasteiger, H. A.; Jakes, P.; Eichel, R. A.; Granwehr, J. Operando Electron Paramagnetic Resonance Spectroscopy-Formation of Mossy Lithium on Lithium Anodes during Charge-Discharge Cycling. *Energy Environ. Sci.* **2015**, *8* (4), 1358–1367.

(27) Shi, F.; Pei, A.; Boyle, D. T.; Xie, J.; Yu, X.; Zhang, X.; Cui, Y. Lithium Metal Stripping beneath the Solid Electrolyte Interphase. *Proc. Natl. Acad. Sci. U. S. A.* **2018**, *115* (34), 8529–8534.

(28) Kim, G.-T.; Appetecchi, G. B.; Montanino, M.; Alessandrini, F.; Passerini, S. Long-Term Cyclability of Lithium Metal Electrodes in Ionic Liquid-Based Electrolytes at Room Temperature. *ECS Trans.* **2010**, *25* (36), 127–138.

(29) Watanabe, M.; Thomas, M. L.; Zhang, S.; Ueno, K.; Yasuda, T.; Dokko, K. Application of Ionic Liquids to Energy Storage and Conversion Materials and Devices. *Chem. Rev.* **2017**, 117, 10, 7190–7239.

(31) Morales-Ugarte, J. E.; Benayad, A.; Santini, C. C.; Bouchet, R. Electrochemical Impedance Spectroscopy and X-Ray Photoelectron Spectroscopy Study of Lithium Metal Surface Aging in Imidazolium-Based Ionic Liquid Electrolytes Performed at Open-Circuit Voltage. *ACS Appl. Mater. Interfaces* **2019**, *11* (24), 21955–21964.

(32) Howlett, P. C.; Brack, N.; Hollenkamp, A. F.; Forsyth, M.; MacFarlane, D. R. Characterization of the Lithium Surface in N-Methyl-N-Alkylpyrrolidinium Bis(Trifluoromethanesulfonyl)Amide Room-Temperature Ionic Liquid Electrolytes. *J. Electrochem. Soc.* **2006**, *153* (3), A595.

(33) Han, X.; Sun, J.; Li, R.; Chemcomm, /; Communication, C. Design of a LiF-Rich Solid Electrolyte Interface Layer through Salt-Additive Chemistry for Boosting Fast-Charging Phosphorus-Based Lithium Ion Battery Performance. Chem. Commun., **2020**, *56*, 6047.

(34) Song, Z.; Wang, X.; Wu, H.; Feng, W.; Nie, J.; Yu, H.; Huang, X.; Armand, M.; Zhang, H.; Zhou, Z. Bis(Fluorosulfonyl)Imide-Based Electrolyte for Rechargeable Lithium Batteries: A Perspective. *J. Power Sources Adv.* **2022**, *14*, 100088.

(35) Tang, Y.; Yu, B. Coinage Metal (Bisfluorosulfonyl) Imide Complexes : Preparation , Characterization , and Catalytic Applications. *Eur. J. Inorg. Chem.* **2020**, 107–118.

(36) Montanino, M.; Alessandrini, F.; Passerini, S.; Appetecchi, G. B. Water-Based Synthesis of Hydrophobic Ionic Liquids for High-Energy Electrochemical Devices. *Electrochim. Acta* **2013**, *96*, 124–133.

(37) Zhou, Q.; Boyle, P. D.; Malpezzi, L.; Mele, A.; Shin, J. H.; Passerini, S.; Henderson, W. A. Phase Behavior of Ionic Liquid-LiX Mixtures: Pyrrolidinium Cations and TFSI- Anions - Linking Structure to Transport Properties. *Chem. Mater.* **2011**, *23* (19), 4331–4337.

(38) Kunze, M.; Jeong, S.; Appetecchi, G. B.; Schönhoff, M.; Winter, M.; Passerini, S. Mixtures of Ionic Liquids for Low Temperature Electrolytes. *Electrochim. Acta* **2012**, *82*, 69–74.

(39) Eshetu, G. G.; Diemant, T.; Grugeon, S.; Behm, R. J.; Laruelle, S.; Armand, M.; Passerini, S. In-Depth Interfacial Chemistry and Reactivity Focused Investigation of Lithium-Imide- and Lithium-Imidazole-Based Electrolytes. *ACS Appl. Mater. Interfaces* **2016**, *8* (25),

16087–16100.

(40) Kerner, M.; Plylahan, N.; Scheers, J.; Johansson, P. Ionic Liquid Based Lithium Battery Electrolytes: Fundamental Benefits of Utilising Both TFSI and FSI Anions? *Phys. Chem. Chem. Phys.* **2015**, *17* (29), 19569–19581.

(41) Biswal, P.; Stalin, S.; Kludze, A.; Choudhury, S.; Archer, L. A. Nucleation and Early Stage Growth of Li Electrodeposits. *Nano Lett.* **2019**, *19* (11), 8191–8200.

(42) Scharifker, B.; Hills, G. Theoretical and Experimental Studies of Multiple Nucleation. *Electrochim. Acta* **1983**, *28* (7), 879–889.

(43) Hou, T.; Yang, G.; Rajput, N. N.; Self, J.; Park, S.-W.; Nanda, J.; Persson, K. A. The Influence of FEC on the Solvation Structure and Reduction Reaction of $LiPF_6$/EC Electrolytes and Its Implication for Solid Electrolyte Interphase Formation. *Nano Energy* **2019**, *64*, 103881.

(44) Maraschky, A.; Akolkar, R. Temperature Dependence of Dendritic Lithium Electrodeposition: A Mechanistic Study of the Role of Transport Limitations within the SEI. *J. Electrochem. Soc.* **2020**, *167* (6), 062503.

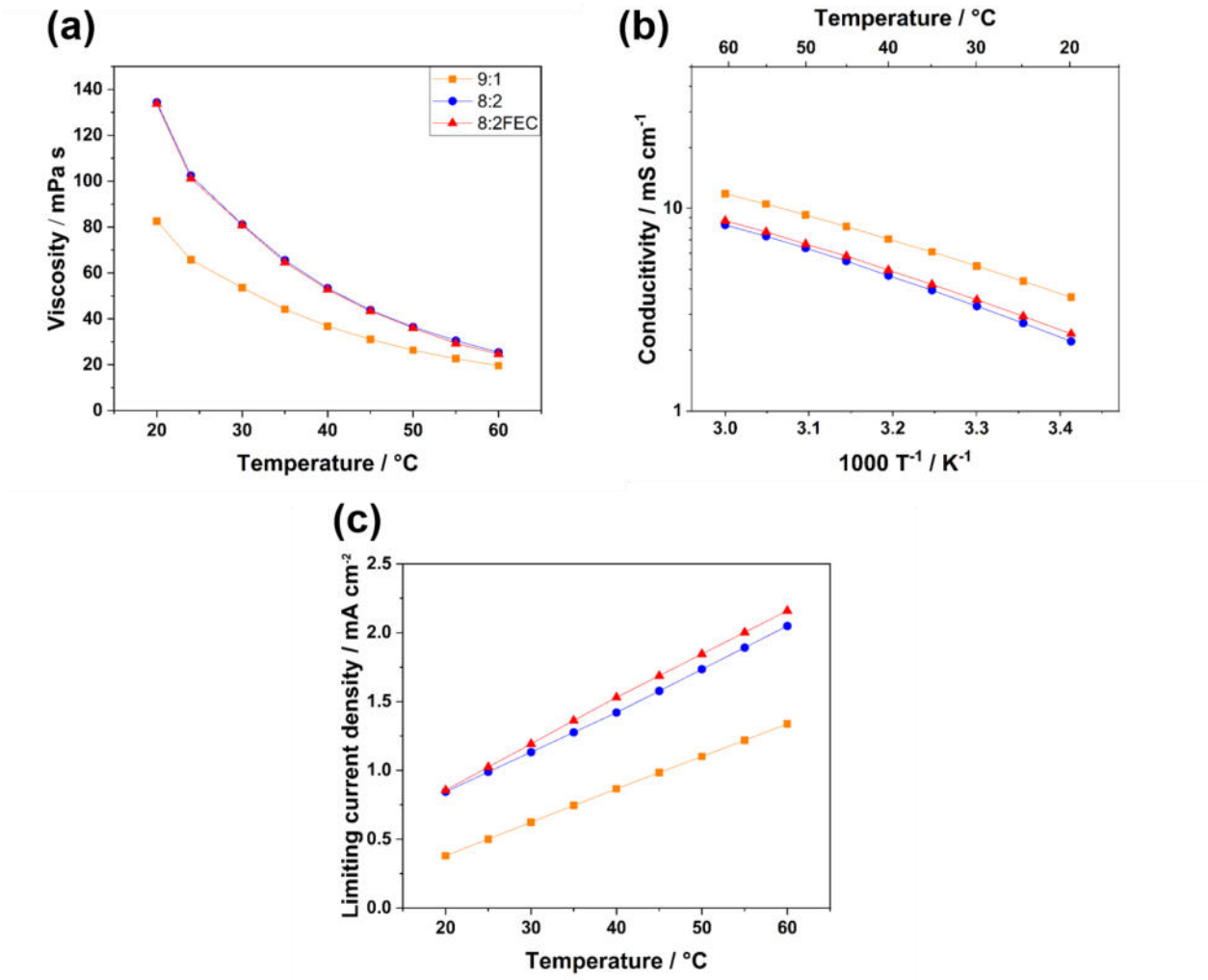

Figure 1. (a) Viscosity, (b) ionic conductivity, and (c) limiting current density of the IL-based electrolytes 9:1 (in orange), 8:2 (in blue), and 8:2FEC (in red) in the temperature range from 20 °C to 60 °C.

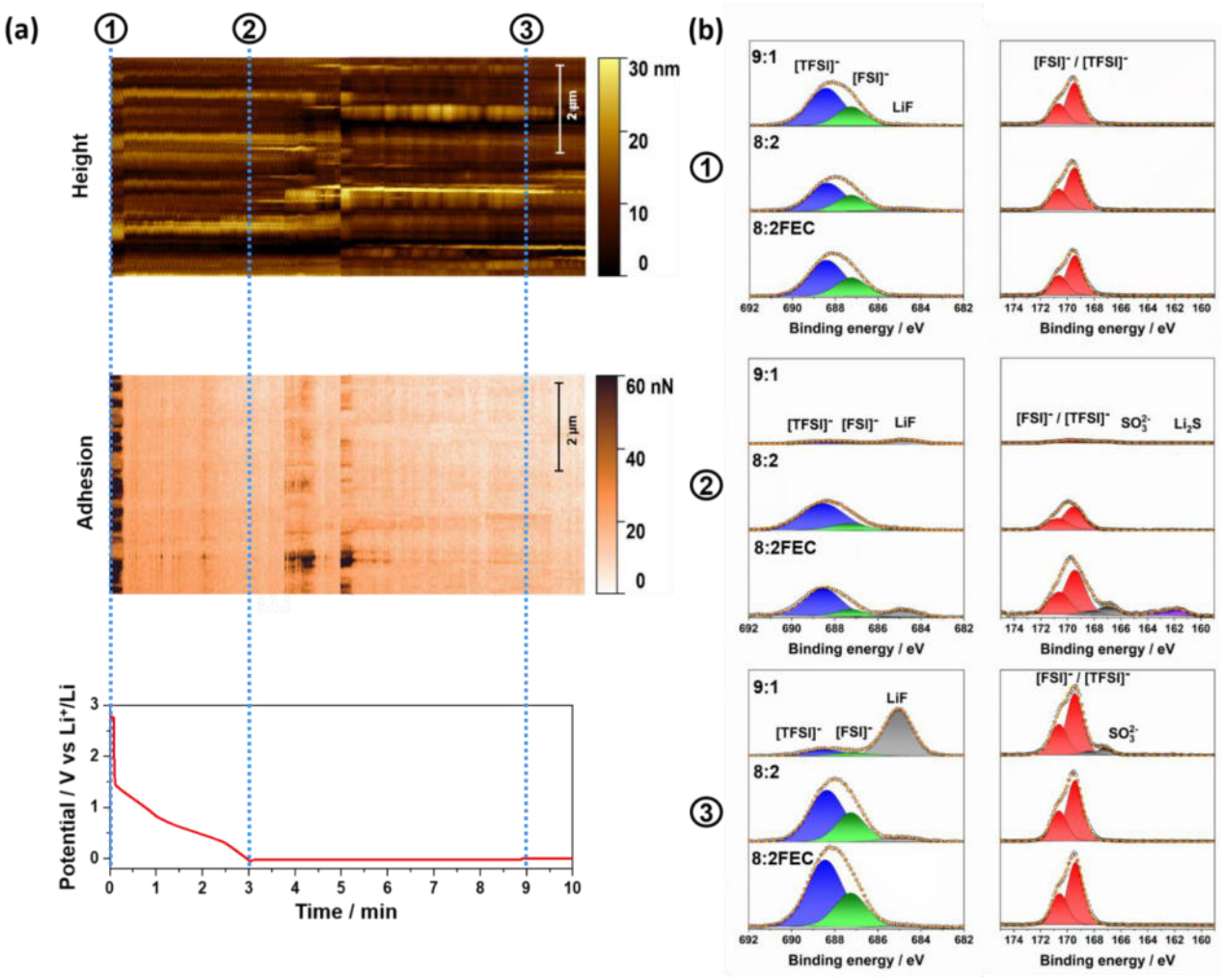

Figure 2. (a) Height, adhesion and potential over time profiles recorded upon lithium plating on a nickel current collector using 8:2FEC (current density: 80 µA cm^{-2}). The images are composed of 5 µm *operando* AFM line scans on the electrode surface, with the slow scan axis switched off. (b) *Ex situ* XPS analysis of the electrode surfaces during the first lithium plating step (stages ①, ②, and ③ in panel (a)) in the three electrolytes (left: F1s; right: S2p).

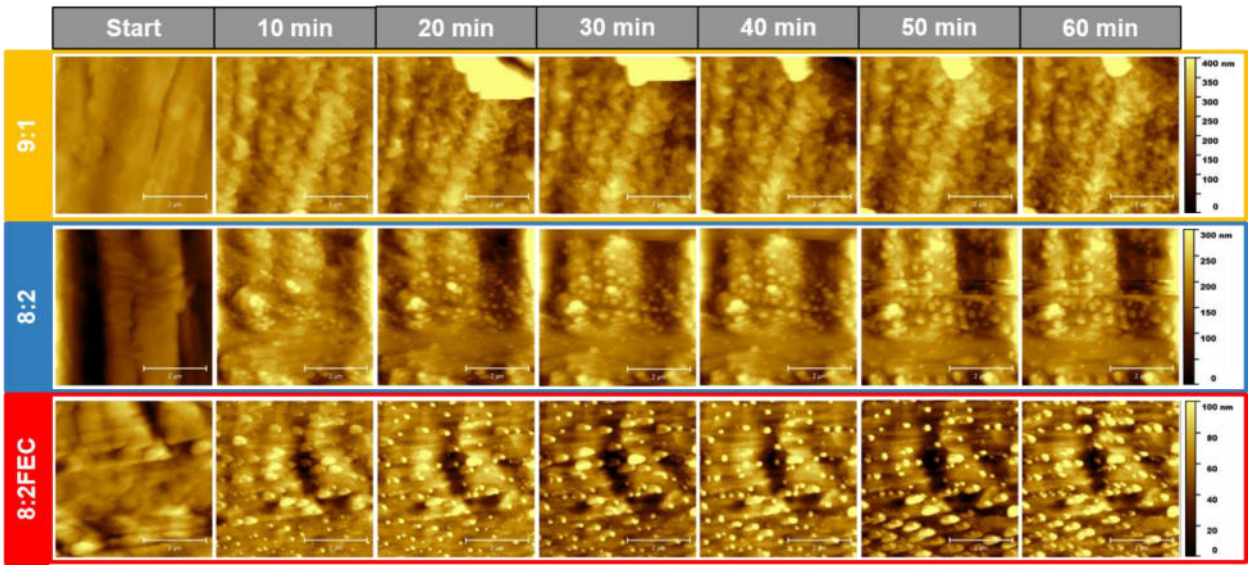

Figure 3. *In situ* AFM mappings (area 5×5 μm^2) of lithium plated onto nickel current collectors at 80 $\mu A\ cm^{-2}$ employing 9:1, 8:2, or 8:2FEC as the electrolyte. The first images on the left show the pristine nickel current collector. The following images demonstrate the evolution of the lithium metal morphology upon plating, with a total plating time increasing from 10 to 60 min in 10 min steps (see also **Figure S2**).

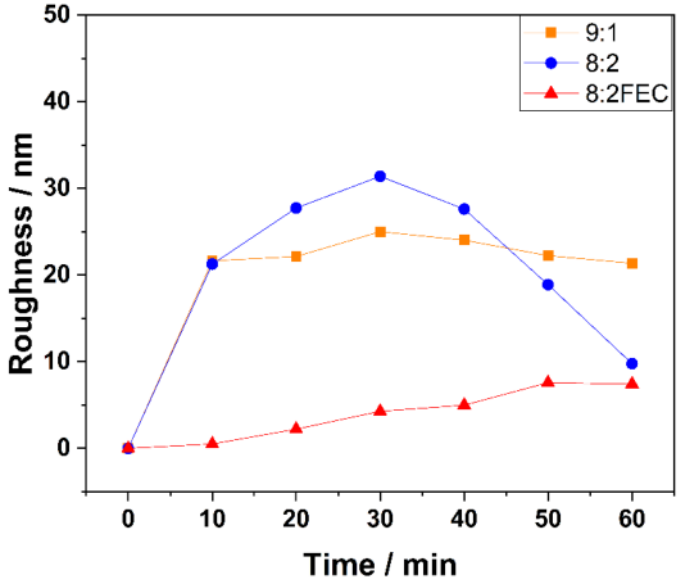

Figure 4. Root mean squared height as a measure of roughness of the lithium metal plated from 9:1 (in orange), 8:2 (in blue), and 8:2FEC (in red), extracted from the in situ AFM mappings presented in **Figure 3**. The values were corrected by subtracting the roughness of the pristine nickel foil at t = 0 min.

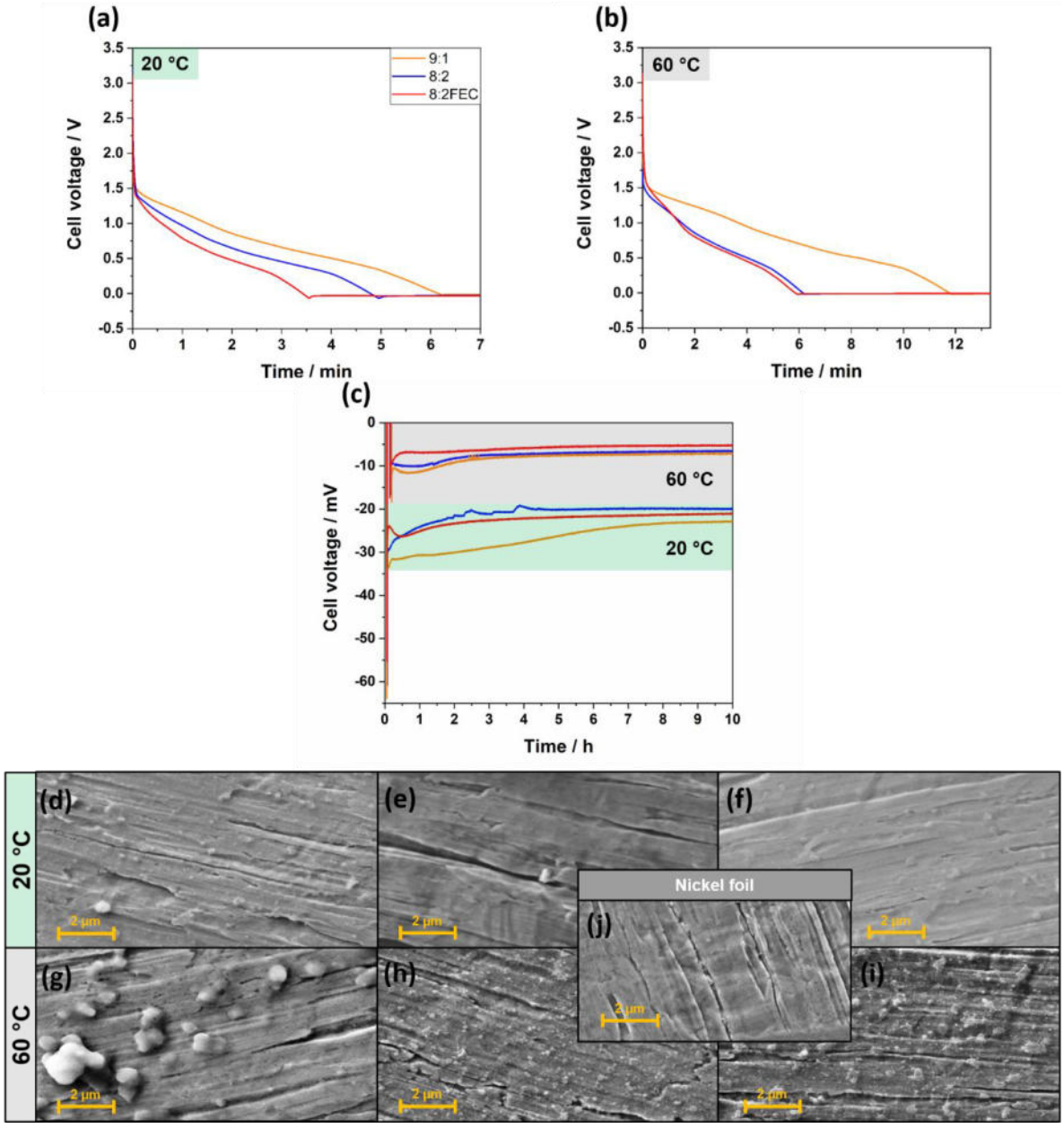

Figure 5. Galvanostatic plating of lithium on nickel current collectors at 80 µA cm^{-2} from 9:1 (in orange), 8:2 (in blue), and 8:2FEC (in red) at (a) 20 °C and (b) 60 °C. (c) Comparison of the complete 10 h plating step for all electrolytes and both temperatures. (d)-(i) *Ex situ* SEM micrographs of the different electrodes when using (d,g) 9:1, (e,h) 8:2, and (f,i) 8:2FEC; the upper ones were obtained after plating at 20 °C, the lower ones after plating at 60 °C. (j) SEM micrograph of the pristine nickel foil for the sake of comparison.

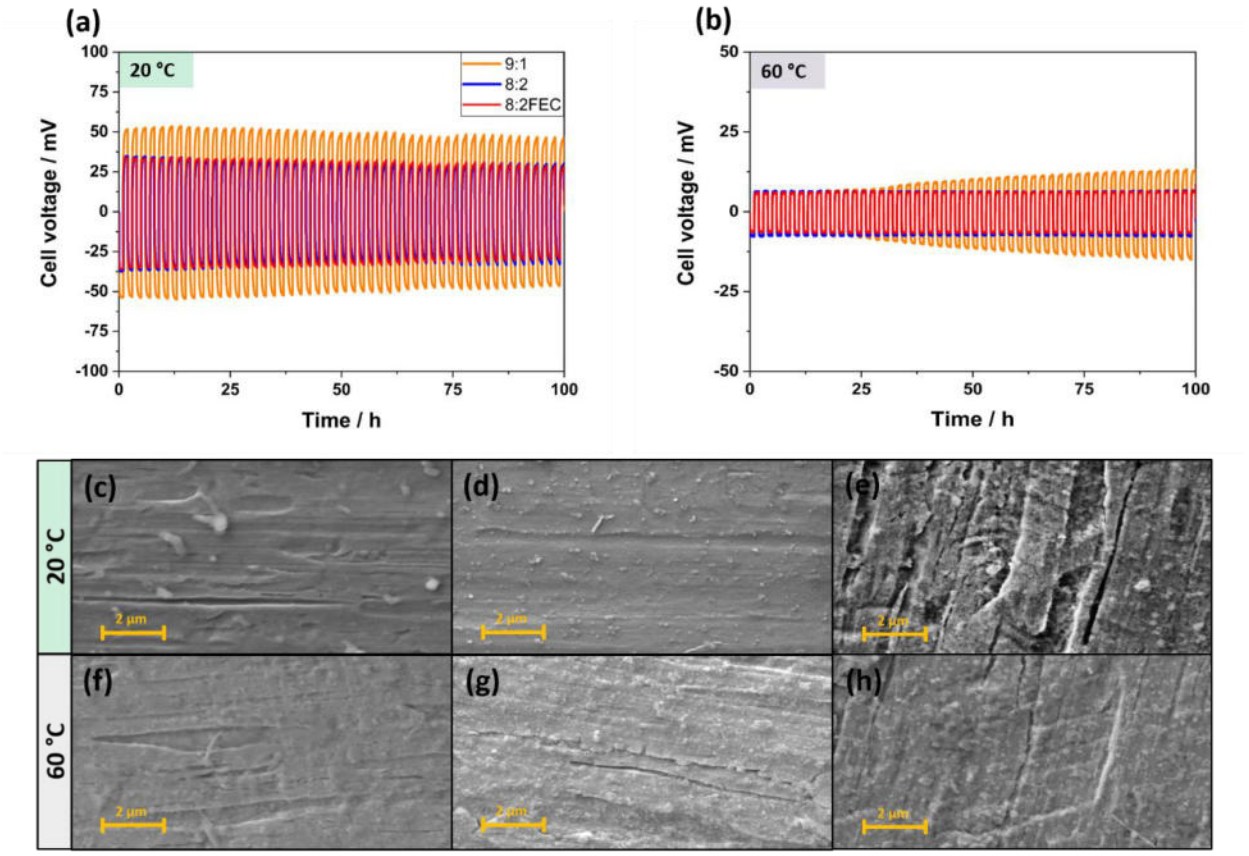

Figure 6. Stripping/plating tests conducted for Li_{Ni}‖Li cells after an initial lithium plating on the nickel current collector (referred to as Li_{Ni}) using the three different electrolyte compositions, i.e., 9:1 (in orange), 8:2 (in blue), and 8:2FEC (in red) at (a) 20 °C and (b) 60 °C at a constant current density of 80 µA cm^{-2}. (c)-(h) *Ex situ* SEM micrographs of the Li_{Ni} electrodes after stripping and plating using (d,f) 9:1, (d,g) 8:2, and (e,h) 8:2FEC.

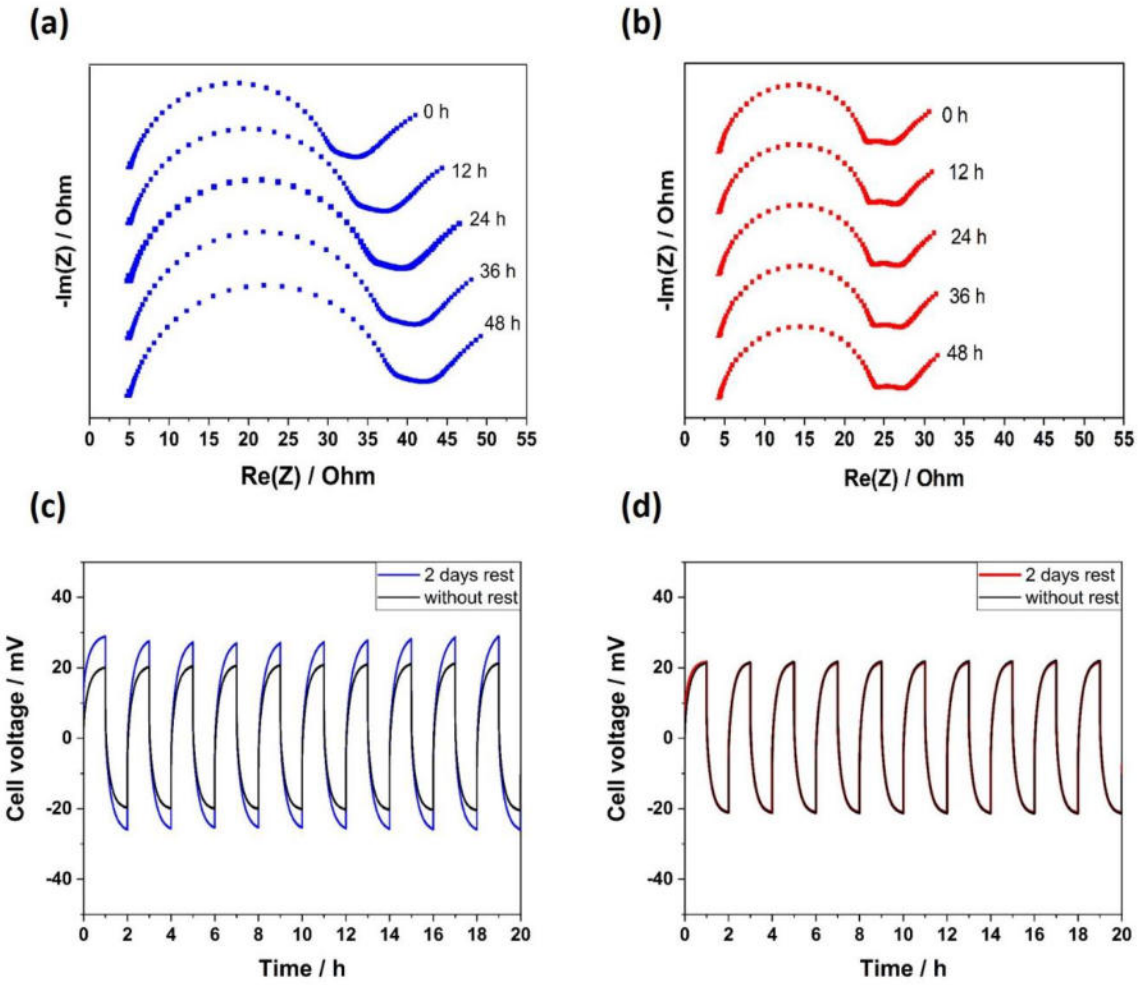

Figure 7. EIS performed on Li_{Ni}‖Li cells after plating lithium for 10 h on the nickel current collector using (a) 8:2 and (b) 8:2FEC during a 2-days rest period with spectra recorded every 12 h. (c) and (d) Comparison of the subsequent lithium stripping and plating of such cells with and without the 2-days rest step when using (c) (8:2) and (d) 8:2FEC.

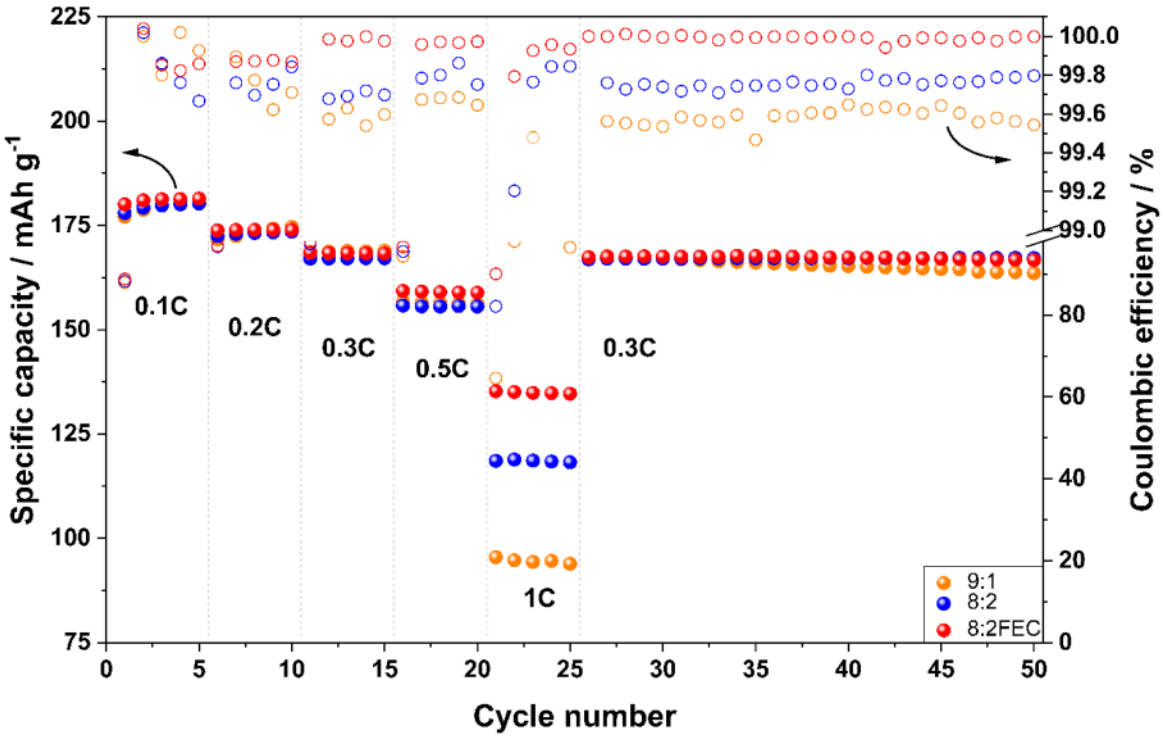

Figure 8. C-rate test conducted with Li‖NCM_{622} cells employing the three different electrolytes, i.e., 9:1 (in orange), 8:2 (in blue), and 8:2FEC (in red) at 20 °C.

ToC Graphic

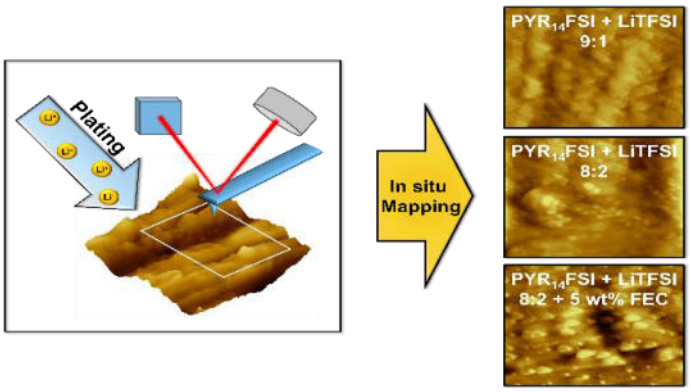
Plating
In situ
Mapping
PYR14FSI + LiTFSI
9:1
PYR14FSI + LiTFSI
8:2
PYR14FSI + LiTFSI
8:2 + 5 wt% FEC

Supporting Information

Insights into the Lithium Nucleation and Plating/Stripping Behavior in Ionic Liquid-based Electrolytes

Dominik Stępień,[1,2] Beatrice Wolff,[3,4] Thomas Diemant,[1,2] Guk-Tae Kim,[1,2] Florian Hausen,[3,4,*] Dominic Bresser [1,2,*] and Stefano Passerini [1,2,5,*]

[1] *Helmholtz Institute Ulm (HIU), 89081 Ulm, Germany*

[2] *Karlsruhe Institute of Technology (KIT), 76021 Karlsruhe, Germany*

[3] *Institute of Energy and Climate Research IEK-9, Forschungszentrum Jülich GmbH, 52425 Jülich, Germany*

[4] *Institute of Physical Chemistry, RWTH Aachen University, 52074 Aachen, Germany*

[5] *Sapienza University of Rome, Chemistry Department, Piazzale A. Moro 5, 00185 Rome, Italy*

*** Corresponding authors:**

dominic.bresser@kit.edu ; stefano.passerini@kit.edu ; f.hausen@fz-juelich.de

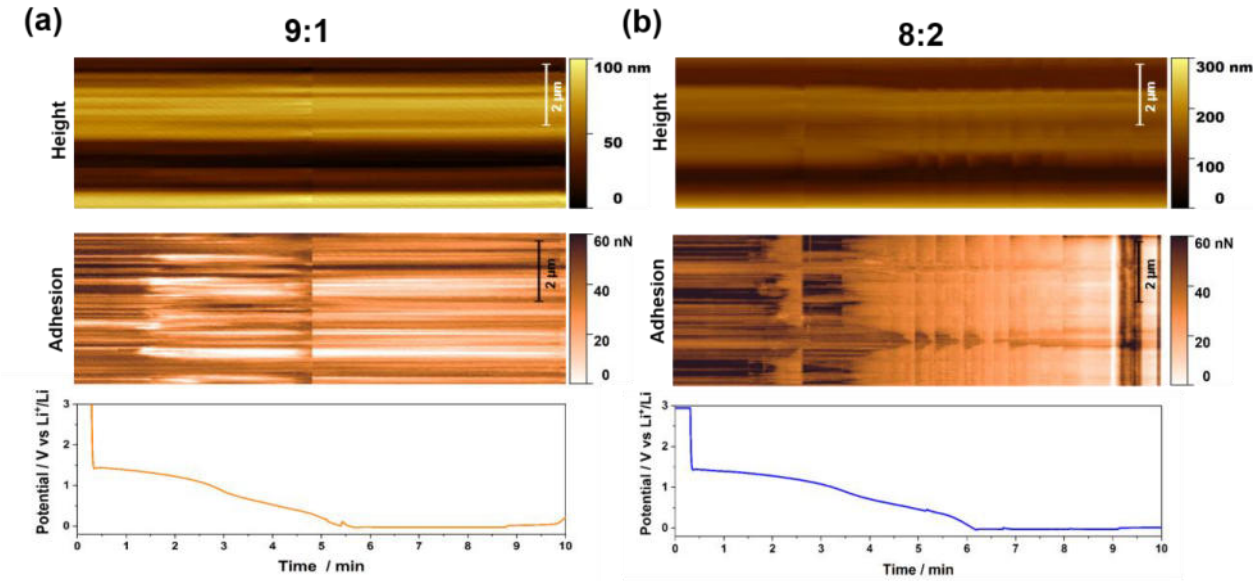

Figure S1. 5 µm *operando* time resolved AFM line scans showing the height and adhesion changes on the nickel current collector while plating lithium at 80 µA cm^{-2} as well as the evolution of the cell voltage as a function of time for (a) 9:1 and (b) 8:2. Please note the different scale bars up to 100 nm for (a) and 300 nm for (b).

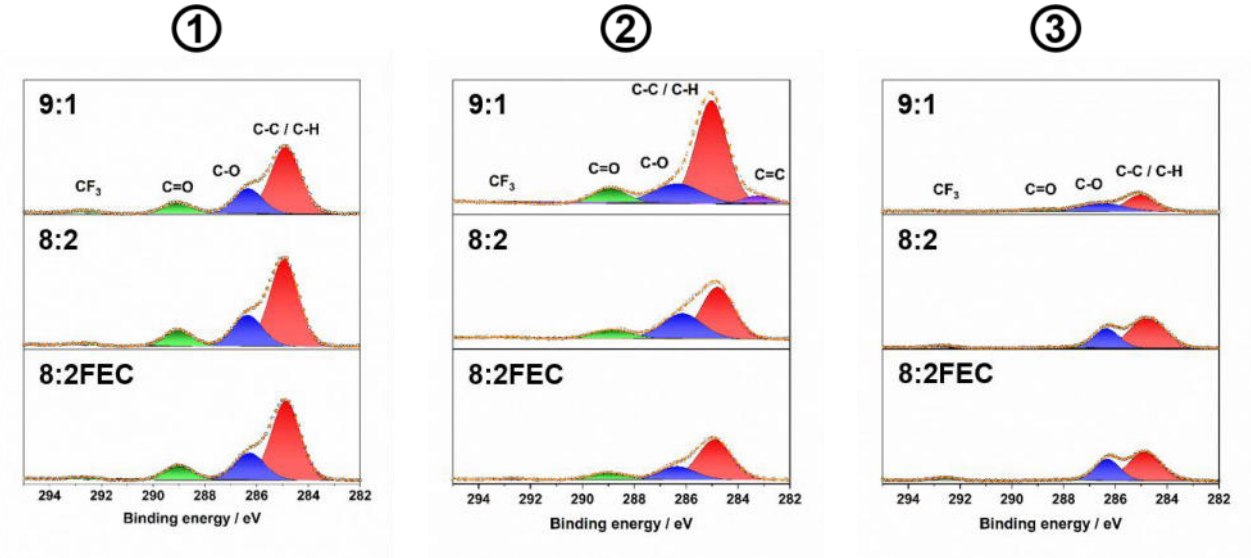

Figure S2. C1s *ex situ* XPS analysis of the electrode surfaces during the first lithium plating step (stages ①, ②, and ③ in panel) in the three electrolytes.

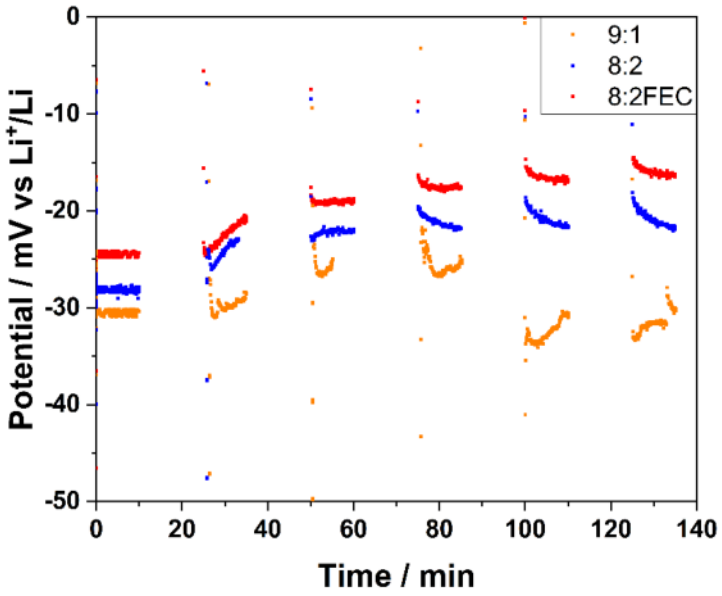

Figure S3. Voltage profiles of the stepwise (each 10 min) lithium plating during the *in situ* AFM mapping experiment (**Figure 3**) using the three different electrolyte compositions, 9:1 (in orange), 8:2 (in blue), and 8:2FEC (in red) at a current density of 80 μA cm^{-2}.

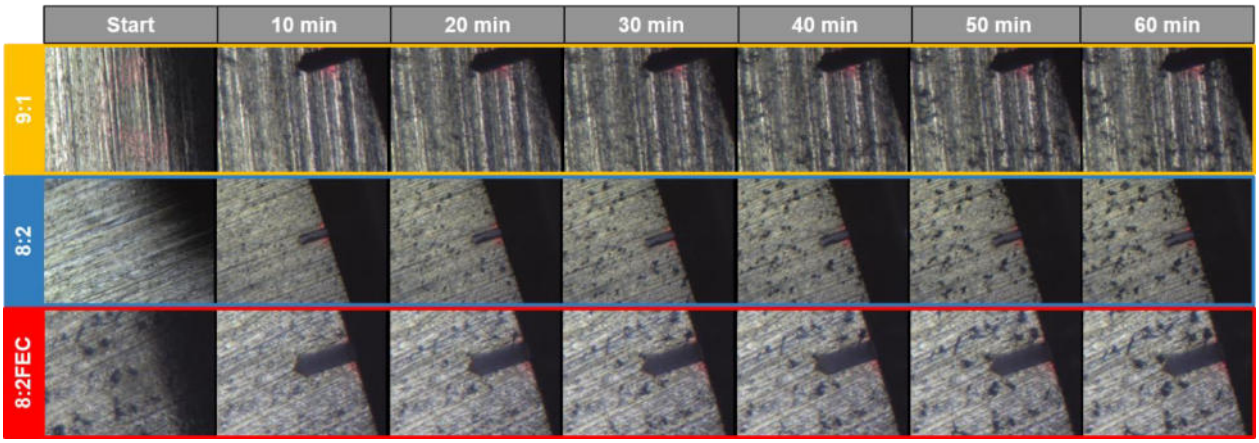

Figure S4. Photographs recorded of the electrode on which lithium was plated during the *in situ* AFM mapping experiment (see also **Figure 3** and **Figure S2**).

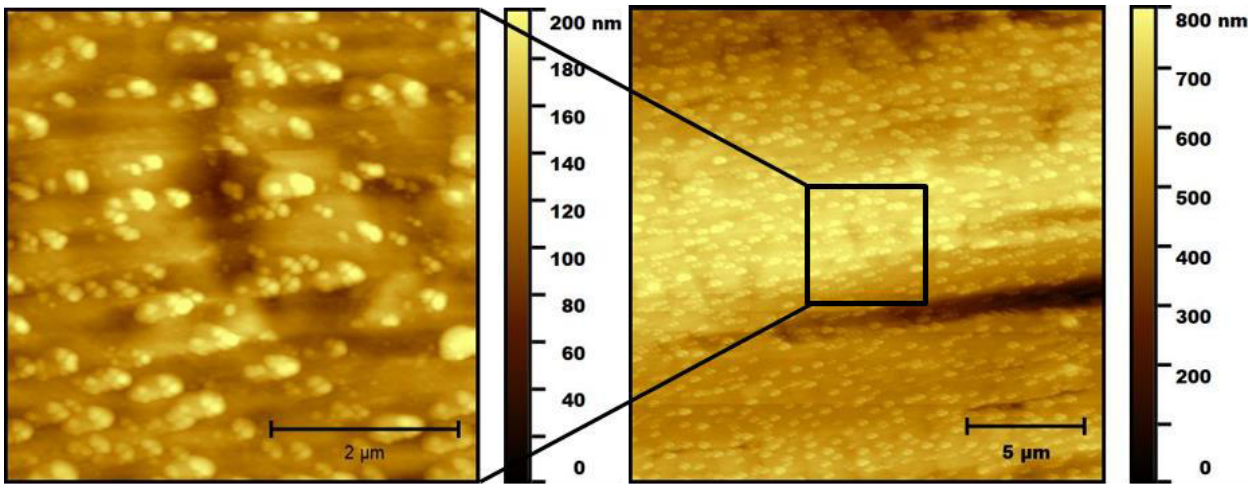

Figure S5. *In situ* AFM surface mapping after 60 min of lithium plating from 8:2FEC. The left panel shows a magnification (5×5 μm^2) of the 20×20 μm^2 area presented in the right panel.

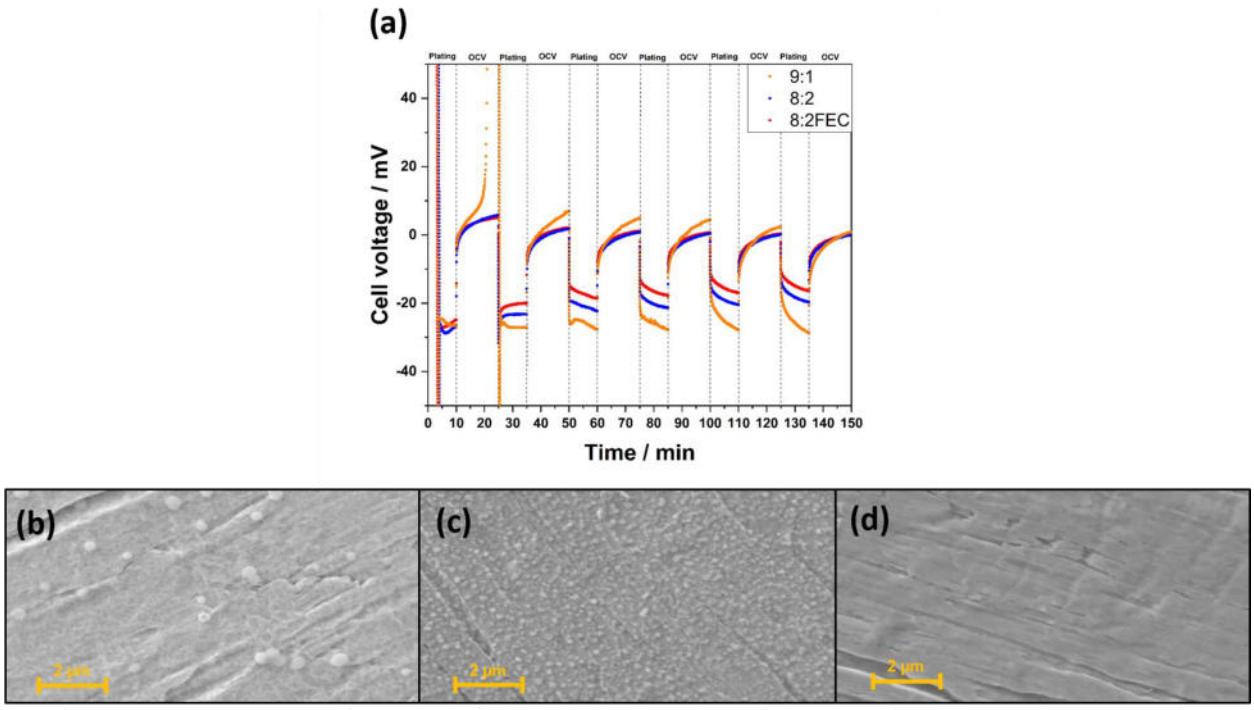

Figure S6. Repetition of the *in situ* AFM mapping experiments in common pouch cells: (a) Plot of the cell voltage as a function of time for the plating and stripping experiment (80 µA cm^{-2}), including OCV steps to represent the time of the *in situ* AFM mapping. (b)-(d) SEM micrographs after 1 h of plating from the three different electrolytes: (b) 9:1, (c) 8:2, and (d) 8:2FEC.

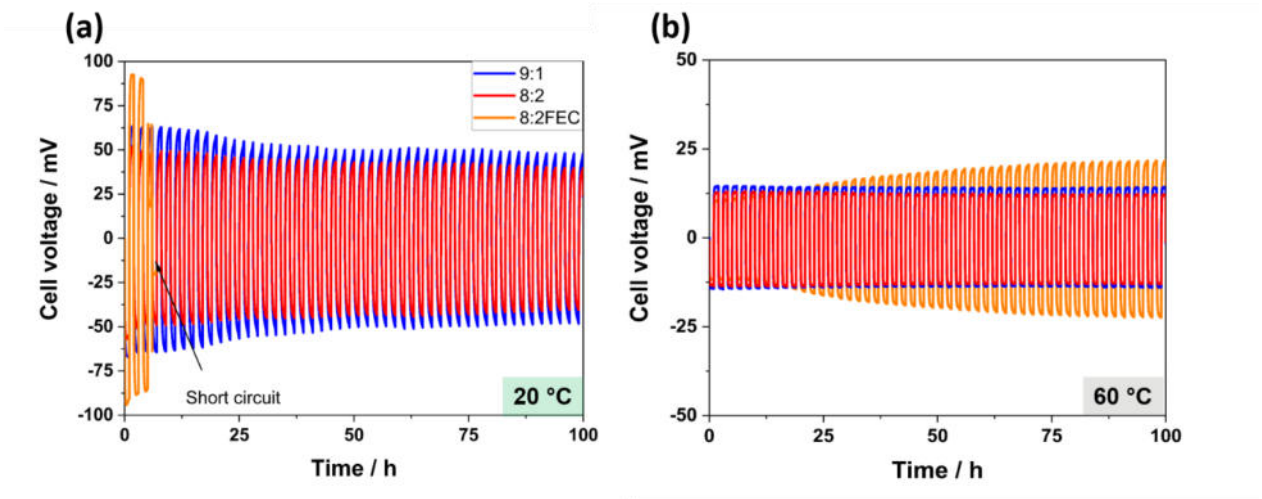

Figure S7. Stripping/plating tests conducted for Li_{Ni}‖Li cells after an initial lithium plating on the nickel current collector (referred to as Li_{Ni}) using the three different electrolyte compositions, i.e., 9:1 (in orange), 8:2 (in blue), and 8:2FEC (in red) at (a) 20 °C and (b) 60 °C at a constant current density of 160 μA cm^{-2}.